Sensors & Diagnostics

PAPER

View Article Online
View Journal | View Issue

Check for updates

Cite this: *Sens. Diagn.*, 2022, **1**, 775

A wearable paper-integrated microfluidic device for sequential analysis of sweat based on capillary action†

Taher Abbasiasl,[a] Fariborz Mirlou, [b] Emin Istif, [a] Hatice Ceylan Koydemir [cd] and Levent Beker [*a]

Soft, skin-mounted microfluidic devices can collect microliter volumes of eccrine sweat and are capable of *in situ* real-time analysis of different biomarkers to assess physiological state and health. Chrono-analysis of sweat can be implemented to monitor temporal variations of biomarker concentrations over a certain period of interest. Conventional methods used to capture sweat or some of the newly developed microfluidic platforms for sweat collection and analysis are based on absorbent pads. They suffer from evaporation, leading to considerable deviations in the concentration of the biomarkers. Here, a paper-integrated microfluidic device is presented for sequential analysis of sweat that is easy to fabricate and does not include air exits for each reservoir, which reduces undesirable effects of sweat evaporation. Furthermore, the high capillary force of filter paper is leveraged to route the liquid into the chambers in a sequential fashion and allow further chemical analysis. The employed design of the paper-embedded microfluidic device successfully samples and analyzes artificial sweat sequentially for flow rates up to 5 μL min^{-1} without showing any leakage. We demonstrated the performance of the device, employing colorimetric assays for chrono-analysis of glucose standard solutions at concentrations in the range of 10–100 mM and pH of sweat during exercise. The results reveal the presented approach's functionality and potential to analyze the concentration of biomarkers over a certain period sequentially.

Received 27th February 2022,
Accepted 24th April 2022

DOI: 10.1039/d2sd00032f

rsc.li/sensors

Open Access Article. Published on 11 May 2022. Downloaded on 2/2/2023 7:07:33 AM.
This article is licensed under a Creative Commons Attribution-NonCommercial 3.0 Unported Licence.

Introduction

Wearable sensors capable of non-invasive analysis of biofluids such as sweat, saliva, interstitial fluid (ISF), and tears have recently gained extensive attention in health monitoring.[1–4] Eccrine sweat, in particular, contains a wealth of different biomarkers, from metabolites and proteins to electrolytes, metal ions, and amino acids,[5,6] and could provide important information regarding physical statuses like dehydration[7] and diseases such as cystic fibrosis and kidney disorders.[8,9] pH level is an important indicator of metabolic alkalosis and a vital parameter in characterizing various health conditions.[10,11] Moreover, glucose level can provide useful information about diet and athletic performance.[12] Early developed technologies for sweat collection rely on absorbent pads or coiled tubes,[13,14] followed by analysis using benchtop equipment. However, expensive laboratory instruments and trained personnel are required to handle this process. Moreover, several personnel-involved steps could result in considerable evaporation, leading to a significant change in the inherently low concentration of different biomarkers in sweat.[9,15] Recent advances in soft, skin-compatible microfluidic devices and chemical sensing techniques have paved the way for novel skin-mounted conformal systems to overcome existing limitations in traditional sweat analysis methods.[16–18]

Several microfluidic platforms have been developed to sequentially analyze different biomarkers in sweat, which enables tracking of temporal variations without interfering with daily activities. One of the most commonly used methods is to use capillary bursting valves (CBVs).[19] Although CBVs can route the sweat effectively, they involve complicated microfabrication processes, including lithography, etching, *etc.*, which require a cleanroom environment. Super-absorbent polymers (SAPs) have also been used as a passive valve to control and guide the sweat into the desired reservoirs for analysis. However, they still need to be coupled with other valves (CBVs or hydrophobic valves) to

[a] *Department of Mechanical Engineering, Koç University, Rumelifeneri Yolu, Sarıyer, Istanbul 34450, Turkey. E-mail: lbeker@ku.edu.tr*
[b] *Department of Electrical and Electronics Engineering, Koç University, Rumelifeneri Yolu, Sarıyer, Istanbul 34450, Turkey*
[c] *Department of Biomedical Engineering, Texas A&M University, College Station, TX 77843, USA*
[d] *Center for Remote Health Technologies and Systems, Texas A&M University, College Station, TX, 77843, USA*

† Electronic supplementary information (ESI) available: Fig. S1–S7. See DOI: https://doi.org/10.1039/d2sd00032f

© 2022 The Author(s). Published by the Royal Society of Chemistry

Open Access Article. Published on 11 May 2022. Downloaded on 2/2/2023 7:07:33 AM.
This article is licensed under a Creative Commons Attribution-NonCommercial 3.0 Unported Licence.

function in sweat chrono-sampling.[15] To reduce the complex fabrication processes, hydrophilic porous media like filter paper and cotton have attracted attention.[20–23] Recent studies utilized the wicking ability of textiles and hydrogel to measure the sweat rate and analyze biomarkers.[22,24–26] However, to the best of our knowledge, this study is the first to implement capillary action for chrono-analysis of biofluids *via* paper-integrated microfluidics. This could eliminate the need for costly, tedious, and time-consuming microfabrication processes. In a study, hydrogel-based thermo-responsive valves were employed to actively route the sweat into the desired reservoirs for analysis.[27] Although their device showed promising results in guiding and compartmentalizing sweat in an active manner, an extra pressure regulation system was needed besides the control valves. Additionally, because of the hydrophobic nature of the microchannels, there is a delay between the target valve opening and the biofluid arrival at the reservoir for sweat analysis.

Filter paper, in particular, has shown great potential in being integrated into microfluidic devices due to easy and low-cost fabrication procedures.[28,29] Because of the high wicking ability of filter paper, when coupled with an active routing system, there is a potential that the delay time would be much lower. Moreover, a lower fluid volume is needed to fill the chamber and come in contact with the sensing system. On the other hand, porous materials can quickly absorb liquid and be utilized as a channel to deliver it to specific points by capillary force. Additionally, filter papers can be integrated with valves to route the liquid into the desirable sensing area.[30]

Herein, we present a simple, robust, and reproducible method to fabricate a microfluidic device that could be used for sequential analysis of sweat. This versatile device can also be integrated into ISF and tear sensing platforms. Filter papers are embedded within a flexible microfluidic device for passive routing of the sweat into the reservoirs sequentially, thereby providing time-dependent analysis of various biomarkers. Moreover, in our design, the reservoirs do not include any air outlet channel for each reservoir. Considering an air exit for each reservoir is problematic because it allows evaporation, thereby changing the concentration of the biomarkers.[9,19,31,32] By only changing the dimensions of reservoir and channel or filter paper type, the device is capable of fluid chrono-analysis for short and long periods. The sweat rate could range from a few hundred nL min^{-1} cm^{-2} (at rest) to about 60 μL min^{-1} cm^{-2} (during severe exercise conditions),[19,33] affecting the required time for sweat to arrive at the sensing area. When conventional microfluidic devices are attached to a body, the biofluid movement inside the microfluidic channels might be affected under extreme conditions such as exercise.[34] However, when using paper inside the microfluidic layer, the capillary force of filter paper ensures that the liquid inside the microchannels always moves towards the desired locations with minimum backflow and intermixing of fluid between different locations. *In vitro* experiments reveal the high potential of the presented approach in *in situ* chrono-analysis at both high (5 μL min^{-1}) and low (<0.5 μL min^{-1}) flow rates. Moreover, the fluid rate measurement part of the device allows an understanding of fluid flow. To demonstrate the performance of the device, the fabricated device is used for chrono-analysis of glucose concentration in an artificial fluid. Also, *in vivo* experiments were performed to determine the pH level in sweat during exercise conditions. The results show the device's functionality in collecting and sequentially analyzing biofluids. Although there has been extensive research on biofluid sensing, this study presents the first work to exploit capillary action for chrono-analysis of sweat and potentially other biofluids.

Results and discussion

Design and fabrication of flexible microfluidic device with embedded filter paper for sequential analysis

An exploded view of the epidermal microfluidic patch for colorimetric sequential analysis of biofluids is presented in Fig. 1(a). The device's overall thickness is 310 μm, developed in rectangular geometry with a length and width of 65 mm and 20 mm, respectively (Fig. 1(b) and (c)). The device comprises layers of patterned and laminated adhesive tape for biofluid analysis and flow rate measurement. Further details about the design of the microfluidic patch can be found in Fig. S1.† A bottom layer of soft ultrathin biomedical adhesive with fluid collection zones at the inlets establishes the route for the liquid to enter the microfluidic channels, provides a strong bond to the skin, and secures sealing. The skin-adhesive layer includes patterns to have an optimum fluid collection while maintaining strong adhesion to the skin. Additionally, three sample collection sites per inlet are utilized to shorten the fluid collection time for the analysis and flow rate measurement parts (Fig. 1(b)). The device was explicitly optimized for sweat collection by considering ~14 sweat glands at 104 glands per cm^2; thus, the collection surface area of each pattern is ~13.4 mm^2 (~40.2 mm^2 collection area for each part of the device).[35,36] Depending on the application, the number of inlets and the surface area of the patterns can be modulated to increase or decrease the fluid collection rate. The star-shaped openings help sweat collection by covering more sweat pores while providing robust attachment of the device to the body. The microchannels and reservoirs were defined using a laser-cutter, which can be programmed by software to rapidly transfer a micro-scale design with high accuracy.

As the sweat enters the device, which is driven by the positive pressure created by natural sweat excretion in the case of sweat sampling,[37] it flows into the microfluidic patch and moves towards the circular reservoirs for colorimetric analysis and the flow rate measurement sections of the patch, simultaneously (Fig. 1(b)). In the case of sweat sampling, the flow rate is an indicator of dehydration level. An increase or decrease in sweat loss affects the concentration of different biomarkers, thus providing crucial information for the analysis of the biomarkers. A thin

© 2022 The Author(s). Published by the Royal Society of Chemistry

Open Access Article. Published on 11 May 2022. Downloaded on 2/2/2023 7:07:33 AM.
This article is licensed under a Creative Commons Attribution-NonCommercial 3.0 Unported Licence.

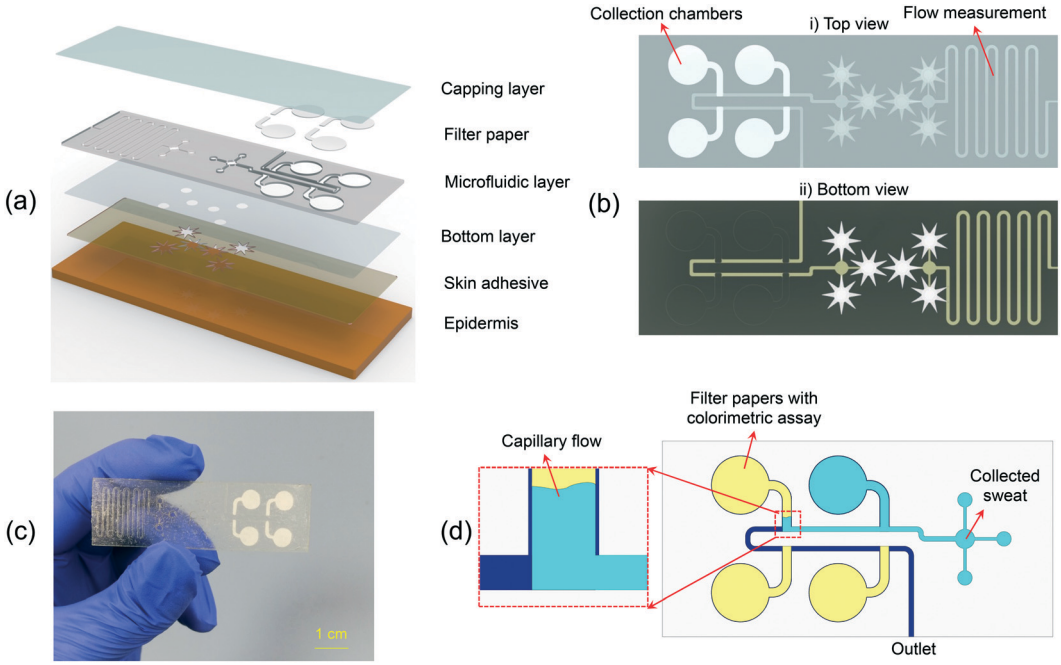


Fig. 1 Schematic illustration of the flexible sensor for chrono-analysis of biofluid. (a) Exploded view of different layers of the sensor. (b) Illustration of top and bottom view of the device. (c) Photograph of the microfluidic device with embedded filter papers. (d) Working principle of the device for sequential analysis.

transparent polyethylene terephthalate (PET) layer encapsulates the microfluidic channel to extract color information from optical images efficiently. The top and bottom view of the device is presented in Fig. 1(b), and an optical image of the representative device is shown in Fig. 1(c). A microfluidic device with four reservoirs, with filter papers embedded in each one, is developed for the sequential sampling of biofluids. The filter paper enables routing of liquid into the reservoirs sequentially by the capillary force, allowing the microfluidic device to be used for effective chrono-analysis of various biomarkers in sweat (Fig. 1(d)).

Theoretical analysis and experimental validation of the filter paper wicking rate

Understanding the fluid behavior in different parts of the microfluidic device enables determining the channel size and the appropriate type of paper (thickness, pore size, *etc.*) to have an optimum design for the required applications. Since the perspiration rate of the human body is different when in rest or during exercise, a suitable design is needed to control the sequential sampling of sweat into separate reservoirs without diffusion-based or flow-based mixing of samples.

The fluid flow in the paper structures is governed by the capillary force at low Reynolds number (Re), which lowers the fluid mixing in straight channels.[38] In dry flow or paper wet-out conditions, where the fluid comes in touch with the paper for the first time, the fluid flow is categorized as laminar flow regime and is modeled by the Lucas–Washburn equation:[39]

$$L = \sqrt{\left(\frac{\gamma r \cos\theta}{2\mu}\right) t} \quad (1)$$

where L is the distance traveled by the fluid front, r is the average pore radius, γ is the surface tension of the liquid, and μ is the dynamic viscosity of the liquid.

Because eqn (1) is only applicable to 1D flow and neglects the effects of hydrophobic boundaries on the capillary flow and evaporation effects, it may lead to a lower accuracy for fluid flow estimation. For a fully wetted paper, Darcy's law can be used to describe the flow rate:[40]

$$Q = \frac{\kappa A \Delta P}{\mu L} \quad (2)$$

Eqn (2) shows that the liquid flow rate (Q) in a fully wetted paper is a function of paper permeability (κ), cross-sectional area (A), pressure difference (ΔP), and dynamic viscosity of the liquid. For the parts of the device where there is no embedded paper, the pressure along the channel can be estimated with the dynamic pressure:

$$P = \frac{1}{2}\rho V^2 \quad (3)$$

where ρ is the density of the liquid and V is the velocity.

By neglecting the pressure loss in the channels, the dynamic pressure can be calculated from the liquid flow rate. When the liquid arrives at the junction points and comes in contact with the filter paper by the pressure difference generated by the biofluid (ΔP_{sw}), the capillary pressure caused by the porous paper (ΔP_{cap}) applies an extra positive pressure and changes the direction of fluid into the reservoir

Open Access Article. Published on 11 May 2022. Downloaded on 2/2/2023 7:07:33 AM.
This article is licensed under a Creative Commons Attribution-NonCommercial 3.0 Unported Licence.

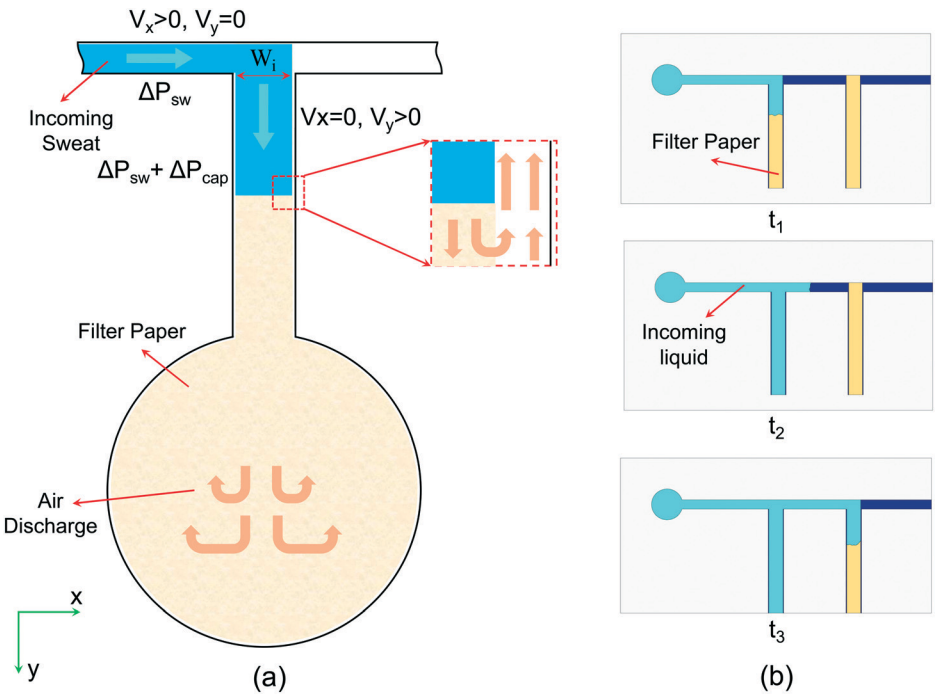


Fig. 2 Schematic demonstration of the working principle of the microfluidic device to route liquid into reservoirs in a sequential manner. (a) Liquid is guided into the reservoir due to the added capillary pressure of filter paper and air discharge (ΔP_{sw}: sweat pressure, ΔP_{cap}: paper capillary pressure). (b) Schematic illustration of chrono-sampling of the liquid.

(Fig. 2(a)). Although the air inside the device might cause a slight pressure loss and slow down the liquid flow, it can come out of the reservoirs through the pores and open spaces between the paper and channel walls and leave the device through the exit at the end of the microfluidic channels. This approach eliminates the need for an air outlet at each reservoir, thereby lowering the rate of evaporation considerably and increasing the accuracy of biomarker analysis.[31] In the study of Zhang *et al.*, one-opening chambers were created using hydrophobic valves to reduce sweat evaporation by removing air outlets.[31] As opposed to this study that used multiple processes to achieve their goal, herein this issue is resolved by simply embedding filter papers in each chamber. The liquid that initially arrives at the entrance section of the first reservoir is pulled by the embedded filter paper into the reservoir because of surface tension. After filling the first reservoir, the liquid starts flowing towards the second reservoir, where the same process occurs (Fig. 2(b)). By this mechanism, all of the reservoirs fill sequentially, enabling chrono-analysis of different biomarkers in biofluids.

To confirm the theoretical approach, an artificial biofluid pumping system was generated to mimic sweat collection (Fig. S2†). The flow rate was varied from 0.5 to 50 μL min^{-1}, corresponding to different sweat rates during resting or exercise conditions.[31,33] In addition, higher sweat rates than those in exercise conditions (0.6 μL min^{-1} per gland)[19,31] were also examined to obtain the maximum flow rate at which the device could perform adequately for sequential analysis. Moreover, the selected double-sided tape for the microfluidic layer has a contact angle of approximately 86°, and based on the equation for capillary pressure ($P_c = (2\gamma \cos\theta/r_c)$,[41] where γ is the liquid–air surface tension, θ is the contact angle, and r_c is the radius, the resulting capillary force on biofluid advancement in the channels is negligible.

The junction points of the paper before reservoirs (depicted as W_i in Fig. 2(a)) should be wide enough so that the capillary force of the paper could change the direction of the liquid. Having the parameters in eqn (1) as $\gamma_{water} = 0.072$ N m^{-1}, $r_{pore} \approx 10$ μm, $\cos(\theta) = 1$ (the water contact angle is approximately 0 on the filter paper), and $\mu_{water} = 0.001$ Pa s, the equation can be simplified as $L = 0.019\sqrt{t}$ (m) $= 19\sqrt{t}$(mm). For liquid flow rates of 0.5–50 μL min^{-1}, the fluid velocity in the microchannels is in the range of 0.11–11 mm s^{-1}. Using eqn (3), the corresponding dynamic pressure will be in the range of 0.006–60.5 mPa, which is much lower than the reported capillary pressures for different filter papers in the literature.[42]

The theoretical analysis of the wicking ability of the filter paper was carried out by dipping a strip of filter paper with width and length of 5 and 100 mm, respectively, into dyed water solution (Fig. S3(a)†), and the required time for the liquid front to travel through the paper at different distances was recorded. The results are presented in Fig. S3(b)† and are compared to the results obtained from the Lucas–Washburn correlation. The considerable difference between experimental and theoretical results was mainly due to the one-dimensional fluid flow assumption in the Lucas–Washburn model. The wicking constant from the experimental results is 4.277 mm $s^{-0.5}$ $\left(L = 4.277\sqrt{t}(\text{mm})\right)$. Using this equation, the time required for the fluid to travel 0.9 mm (width of the filter paper) through the

© 2022 The Author(s). Published by the Royal Society of Chemistry

Open Access Article. Published on 11 May 2022. Downloaded on 2/2/2023 7:07:33 AM.
This article is licensed under a Creative Commons Attribution-NonCommercial 3.0 Unported Licence.

strip is 0.044 s. To change the direction of the liquid when it comes in contact with the paper, the fluid velocity in the x-direction needs to reach 0 at the end of the strip (Fig. 2(a)). By using $\bar{V} = \Delta x/\Delta t$ from the above information, the resulting average velocity is 20.4 mm s^{-1}, and based on the cross-sectional area of the microchannels, the corresponding liquid flow rate would be 104 μL min^{-1}. This means that the capillary pressure of the paper creates enough driving force to change the direction of fluid flow from the x- to the y-direction for flow rates up to 104 μL min^{-1}. However, it should be noted that the traveling rate of the liquid front diminishes over time. By assuming the embedded paper in each reservoir as an equivalent strip with 0.9 mm width, the required time for the liquid to travel 0.9 mm at the end of the strip is 6.7 s. The resulting average velocity and liquid flow rate would be 0.134 mm s^{-1} and 0.68 μL min^{-1}, respectively, which reveals a significant decline in the efficiency of the paper strip in guiding the liquid. Nevertheless, even at this flow rate (0.68 μL min^{-1}), the device would be effective for extreme cases.

Although the force due to surface tension might be sufficient to pull the fluid towards the desired reservoir, the capillary pressure of paper diminishes as the fluid moves inside the paper as a result of viscous resistance, which is proportional to the velocity with $8\mu L/D^2$.[43] This resistance force causes a reduction in fluid velocity as the liquid front moves through the porous paper, as the calculated velocities above also confirm. According to the characterization results, at the beginning of liquid and paper contact, the porous medium could also pull a high flow rate of liquid (*e.g.*, 25 μL min^{-1}) and change its direction. However, this lasts for only a short duration, and after that, the liquid continues its original direction while also penetrating the paper.

Effectiveness of paper wicking under different flow rates

The proposed device will only be effective up to a certain flow rate, based on the design of the filter paper.[43] To investigate the performance of the proposed paper-based device at different liquid flow rates, a simple design was used. Red and blue dyes were located near the inlet of the channels to facilitate visualization of the filling process. In Fig. 3(a), the liquid flow rate is 0.5 μL min^{-1}, and our data suggest that the paper width of 0.9 mm is sufficient to guide the liquid entirely into the reservoir. Using $\left(L = 4.277\sqrt{t}(\text{mm})\right)$, the required time for the liquid to travel through the whole paper and final 0.9 mm is 2.16 and 0.57 s, respectively. By using $\bar{V} = \Delta x/\Delta t$, the required time for the velocity of the flow to reach zero in the x-direction when it comes in contact with the paper is about 8.18 s, which is much longer than 0.57 s. Therefore, the liquid stops at the intersection (Fig. 3(a)-II) until the liquid fills the first section completely. As shown in Fig. 3(a)-III, the liquid continues its movement in the x-direction after complete filling of the first section (the red-colored liquid has reached the end of the paper). When the liquid arrives at the second intersection, the liquid velocity in the x-direction becomes zero again, and the filter paper pulls the flow into the second section until the second section fills, after which the fluid continues its movement in the x-direction towards the exit (Fig. 3(a)-IV and V).

To investigate the device performance at higher sweat rates, a liquid flow rate of 5 μL min^{-1}, corresponding to a sweat rate of ~0.12 μL min^{-1} per gland, was pumped into the microfluidic device using the artificial perspiration system. As shown in Fig. 3(b)-II, the fluid velocity reaches zero in the x-direction, and the filter paper guides the liquid into the

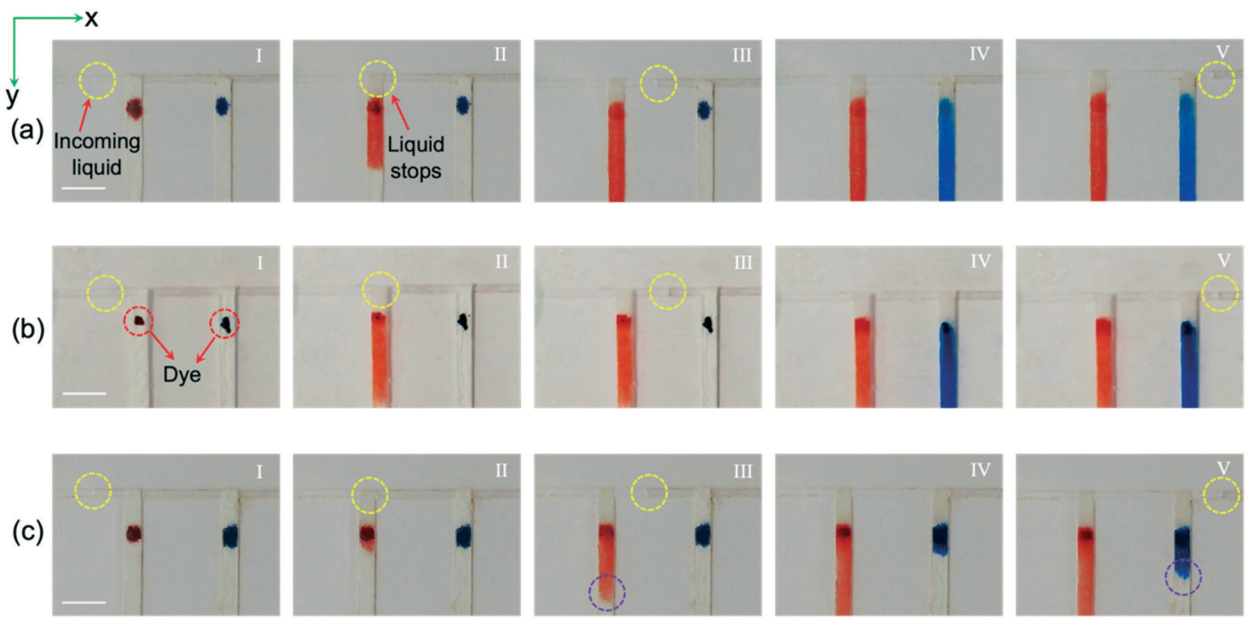


Fig. 3 A simple design of the microfluidic device with embedded filter papers to show the approach could work at different liquid flow rates corresponding to different sweat rates. (a) 0.5 μL min^{-1}, (b) 5 μL min^{-1}, (c) 25 μL min^{-1} over time (I–V). Scale bars represent 2 mm. Yellow circles: uncolored liquid flow front. Purple circles: colored liquid flow front.

Open Access Article. Published on 11 May 2022. Downloaded on 2/2/2023 7:07:33 AM.
This article is licensed under a Creative Commons Attribution-NonCommercial 3.0 Unported Licence.

first section. For the flow rate of 5 μL min^{-1}, 0.82 s is needed for the flow to reach zero velocity in the *x*-direction, which is higher than 0.57 s, the required time for the fluid front to travel the final 0.9 mm of the paper strip. The fluid continues its movement in the *x*-direction after filling the first section, and when it arrives at the second paper strip, the whole process repeats until the fluid exits through the outlet (Fig. 3(b)-III–V). In Fig. 3(c), the device's applicability at a flow rate of 25 μL min^{-1} corresponding to a sweat collection area of ~40 mm^2 at 104 glands per cm^2 and sweat rate of 0.6 μL min^{-1} per gland was examined. At the beginning of paper wet-out, the liquid travels quickly through the paper, and it stops the liquid movement in the *x*-direction (Fig. 3(c)-II). However, after some point, the rate of liquid movement in the paper drops, and some part of the liquid starts moving in the *x*-direction while also filling the remaining part of the first section (Fig. 3(c)-III). At a flow rate of 25 μL min^{-1}, ~0.16 s is required for the liquid to stop entirely at the *x*-direction, which is lower than 0.57 s, and as a result, after filling a part of the first channel (~2 mm), the liquid continues flowing in the *x*-direction. As shown in Fig. 3(c)-IV and V, the same process occurs when the liquid arrives at the second intersection. Although it is realized that the presented paper-based device may not function properly at very high flow rates, the examined liquid flow rates in the inlet are well within the sweat rate range available in the literature.[19,31,33] Moreover, by simply increasing the width of the filter paper or making other possible alterations, the device's applicability for higher flow rates can be enhanced. Previous studies showed that the transfer time of the liquid to the sensing area is reduced by increasing the width of the paper.[44] Since a part of the filter paper in the proposed device is placed in the main microchannel to wick the fluid into the reservoirs, it should be noted that by selecting wider substrates, the pressure drop will be increased in the main channel. This could result in a liquid leakage, backflow, and fluid blockage. To avoid this issue, our experiments showed that for flow rates of up to 10 μL min^{-1}, there will not be any leakage or fluid blockage for the paper width of 0.9 mm. The paper diameter for the chamber section is 6 mm, which is in the range of other paper-based devices with colorimetric analysis.[44–46] It is also worth mentioning that decreasing the width of the filter paper (to decrease the pressure drop) reduces the ability of the device in changing the direction of the incoming liquid in the main microchannel into the sensing chamber.

Fluidic operation of the paper-integrated microfluidic device for the sequential sampling of sweat

Sequential fluid sampling was accomplished by embedding filter papers in the microfluidic layer, which allows chrono-analysis of biofluids without any actuator or moving part. Fig. 4 illustrates how the device successfully collects liquid into separate reservoirs without undesired flow mixing. Red, blue, green, and purple dyes are located near the inlet of

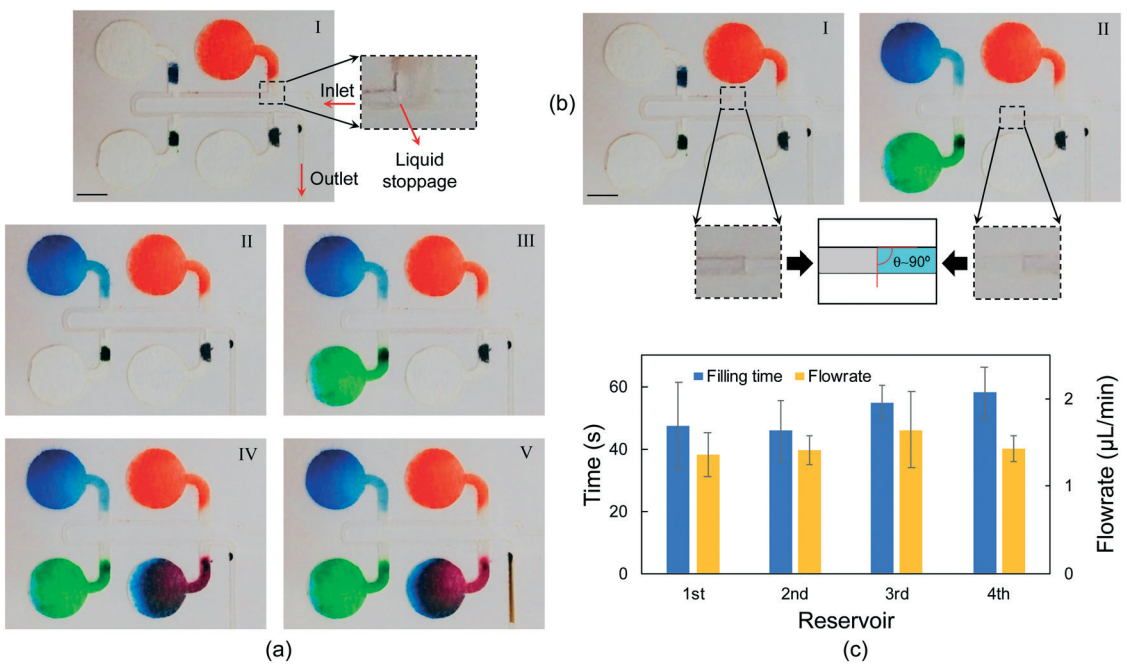


Fig. 4 Sequential filling of the microfluidic device at a pumping flow rate of 1.5 μL min^{-1}. (a) *In vitro* chrono-sampling of liquid on paper-embedded chambers dyed with different colors: (I) filling the first reservoir (red-dyed) and liquid stoppage at the junction, (II) filling the second reservoir (blue-dyed), (III) filling the third reservoir (green-dyed), (IV) filling the fourth reservoir (purple-dyed), and (V) liquid flowing through the exit channel (brown-dyed). (b) Wetting angle of the liquid in different locations of the microchannels: (I) between the first and the second reservoir and (II) between the third and the fourth reservoir. (c) The time required to fill each reservoir and measured liquid flow rate after each reservoir. Scale bars represent 3 mm.

© 2022 The Author(s). Published by the Royal Society of Chemistry

Open Access Article. Published on 11 May 2022. Downloaded on 2/2/2023 7:07:33 AM.
This article is licensed under a Creative Commons Attribution-NonCommercial 3.0 Unported Licence.

each reservoir to facilitate the visualization of chrono-filling. Also, a brown dye is located at the outlet to visualize the exiting flow from the device. Since the dimensions of microchannels are in hundreds of micrometers and the flow rates were a few microliters per minute, the Reynolds numbers are smaller than 1 (Re <1), which suggests that the flows in the device are laminar and only diffusion-based mixing occurs.[47,48] In Fig. 4, sequential filling of sweat into the micro-reservoirs is demonstrated at a flow rate of 1.5 μL min^{-1}, which could be considered a high flow rate compared to physiological ranges of sweat rate.[49] Four reservoirs are considered to monitor the concentration of biomarkers at four different time frames. No actuator or external part is used, and sequential sampling is simply achieved by embedding filter papers inside the microchannels. Furthermore, unlike many studies that have considered exit channels for each reservoir to allow the air inside the reservoir to leave,[9,19] in this method, the need for an air outlet for each reservoir is eliminated, which results in lower water evaporation and more accurate concentration analysis of biomarkers. Despite the high liquid flow rates, no liquid leakage was observed during the sampling (Movie S1). This suggests that the fluid can advance easily in the different parts of the device without any liquid blockage, resulting in increased pressure and leakage.

In Fig. 4(a)-I, the liquid has filled the first reservoir (red dye), and the flow is completely stopped at the junction of the first reservoir. The flow does not start to move towards the second reservoir without the first one entirely filled, which shows that the air inside the reservoir exits from the chamber completely. This is especially beneficial for the sequential sampling of biofluids because with every reservoir being entirely filled, the liquid from the following time frames will only flow towards the next reservoirs, enabling chrono-analysis of the biofluid. After filling the first reservoir, the liquid flows towards the second reservoir, and the same process repeats for the third and fourth reservoirs (Fig. 4(a)-II to IV and Movie S1†). The high capillary action of the filter paper lowers the intermixing between the reservoirs considerably (*i.e.*, no colored dye is transferred to other chambers by flow). This shows the advantage of the employed method over the paper-based devices integrated with dissolvable valves in liquid chrono-sampling.[30] Moreover, the interfaces between chambers with different colors are less than 5% of the total volume of each chamber, leading to low molecular diffusion between reservoirs. In this sequential sampling approach, there is a considerable improvement over previous studies in reducing the intermixing between reservoirs.[19,31] The color gradient in Fig. 4(a) is caused by the fluid flow during chamber filling. Increasing the binding of the color or enzyme in the case of enzymatic analysis of biomarkers could help overcome this issue.[45,50] Moreover, the color gradient is lower in some reservoirs. This is mainly because the amount of dye placed in the entrance section of the paper is higher compared to that in the other reservoirs. This result suggests that although challenging, non-uniform spotting of the reagents during preparation of the colorimetric assay could help in reducing the color gradient. In our microfluidic device, reagents are spotted in the entrance section of the circular zones so that higher enzyme attachment could happen in this section and liquid flow could carry along the unattached enzymes, resulting in a more uniform color after enzymatic reaction. For further enhancement, a higher concentration of reagents could be spotted on the fluid entrance section. By doing this, a part of the reagents in this part could be transferred to other parts (lower concentrations of reagents), leading to a more uniform color. Fig. 4(b) shows close-up images of the liquid shape and wetting angle in the microchannels. The wetting contact angle is about 90° at different locations of the device (Movie S1†), which suggests that the effect of capillary force inside the channels on liquid advancing is almost negligible. The required time for each reservoir to be filled (the time difference between liquid arrival and flowing towards the next chamber) is presented in Fig. 4(c). All the chambers are roughly filled at the same duration, and the minor difference in the required time to fill each chamber could be because of small deformations or compressions on the filter paper during the fabrication process, which affects the liquid traveling speed in the paper.[51] According to Fig. 4(c), the average required time for the reservoirs to be filled is about 51.5 s. However, it takes ~3.3 min for the reservoirs (~5 μL volume without filter paper) to be filled at the same flow rate. This suggests that the analysis time could be lowered significantly when needed (*e.g.*, electrochemical sensing, which needs the entire reservoir to be filled to ensure complete contact between the liquid and the electrodes) by embedding filter papers in the reservoirs. The measured liquid flow rate after each reservoir is approximately equal. The minor variations might have resulted from early or late detachment of liquid from the filter paper. When the liquid detaches earlier, as discussed in the theoretical analysis, it means that the reservoir is yet to be filled, and as a result, the reservoir continues to be filled after liquid detachment, leading to a lower flow rate after the reservoir.

Flow rate measurement and evaporation rate

Measuring sweat rate is an essential indicator of dehydration and kidney disorders. Several methods have been proposed to measure sweat rate, including electrical impedance,[33,52,53] capacitance hygrometry,[54] and, recently, the kinetics of liquid filling into the microfluidic device.[46] Herein, the latter was used to measure the fluid flow rate. Blue-dyed water was pumped into the microfluidic layer using the syringe pump in the test setup (Fig. S2†). Fig. 5 shows the filling process of the flow rate measurement part of the microfluidic patch at a flow rate of 5 μL min^{-1}. Fig. 5(a) and S4† demonstrate the required time to advance the fluid in the microchannels. A wetting contact angle of about 90° was observed (Movie S2†). The volume inside the channels can be measured at different

Open Access Article. Published on 11 May 2022. Downloaded on 2/2/2023 7:07:33 AM.
This article is licensed under a Creative Commons Attribution-NonCommercial 3.0 Unported Licence.

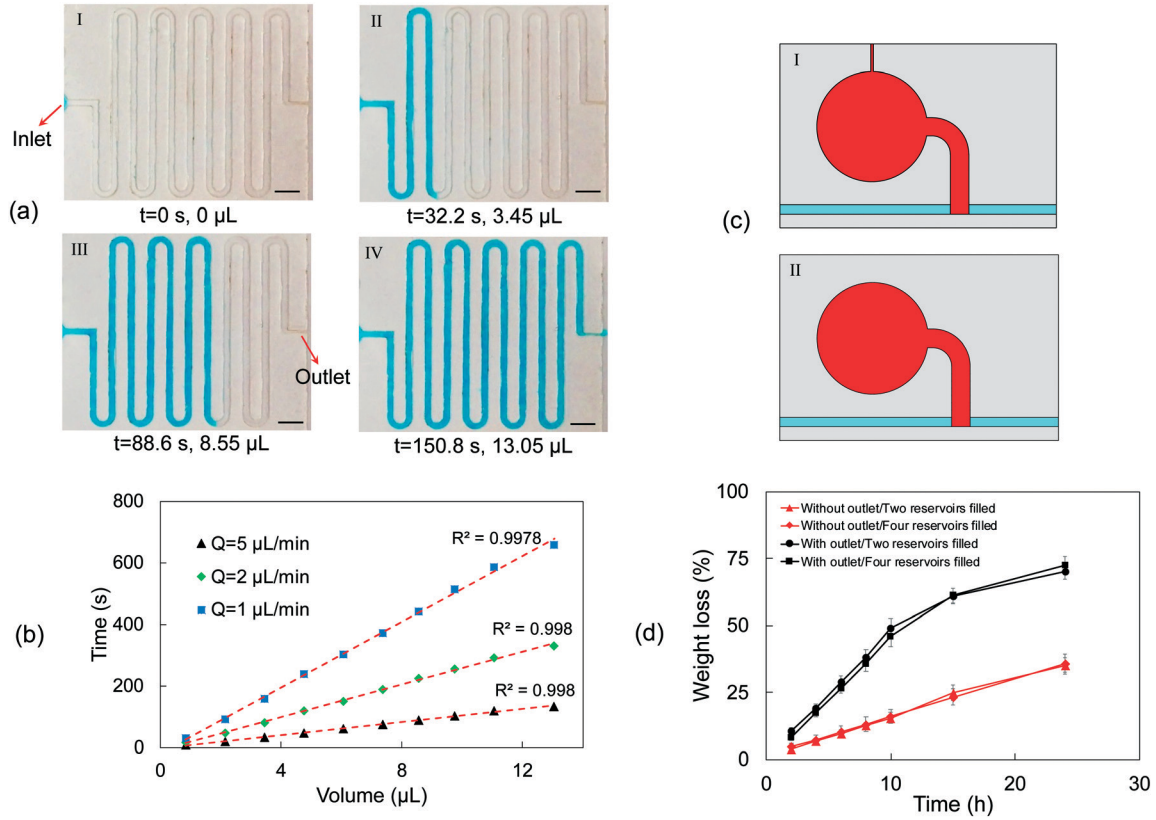


Fig. 5 (a) Liquid advancement in the microchannels over time at a liquid flow rate of 5 μL min^{-1} over time (I–IV). (b) Measured liquid volume inside the device over time at three different flow rates. Scale bars represent 2 mm. (c) (I) Reservoir with an air outlet, (II) reservoir without an air outlet to study the reduction of evaporation rate for the microfluidic device without an air outlet. (d) Measured evaporation rate for the devices with and without an air outlet, indicating a clear reduction in the water loss by removing the air outlet.

time frames using the optical images and can be used to measure the flow rate. In Fig. 5(b), the volume of liquid inside the device over time at different flow rates is given. The measured flow rates show good consistency over time, indicating that the adopted method could serve as a good choice of measurement of the biofluid flow rate.

Owing to the inherently low concentration of different biomarkers in sweat, it is of high importance to preserve the liquid content in the solution to avoid any concentration change because of evaporation. Special design of the microfluidic device in this study eliminated the need for air outlets. Fig. 5(c) shows the reservoirs with (I) and without (II) a 150 μm wide air outlet. The mechanism of air discharge in the case of no air outlet was explained in the previous sections. The water weight loss was determined by measuring the initial weight of the device and the weight of the device at different times. A high-precision balance was used to measure the weight difference at 37 °C to simulate the evaporation rate when the device is attached to the body. Although water weight loss can be seen for the case of no air outlet in Fig. 5(d), there is a significant decrease in the rate of water loss compared to the devices with air outlets. This proves the lower evaporation rate by removing the air outlets, thus lowering the inaccuracy of biomarker concentration analysis. As can be seen in Fig. 5(d), the evaporation rate is almost the same when two or four reservoirs of the device are filled. After two days there was still water left in the reservoirs for the device with no air outlets, whereas the device with air outlet was completely dried out (Fig. S5†). The low evaporation rate is especially vital for small biofluid collection rates. Although the evaporation rate is smaller compared to those of previous studies,[31] extra efforts are needed to further reduce the evaporation. It is already challenging to collect sweat at low perspiration rates (*e.g.*, at rest),[33] and evaporation of collected sweat would make it even harder and lower the accuracy of analysis.

Chrono-analysis of glucose concentration and pH

For quantitative *in vitro* testing of the performance of the microfluidic device, standard glucose solutions at different concentrations were sequentially pumped into the device using the syringe pump (Fig. S2†). Here, a colorimetric sensing approach is employed for simple and rapid assessment of glucose concentration. Several studies have used paper-based chemical assays for the colorimetric analysis of different biomarkers in sweat.[31,32,46,55] Optical images were collected from a series of experiments with samples of known glucose concentrations for calibration purposes. An open-source image analysis software (*i.e.*, ImageJ) was used to extract the intensity profiles at R, G, and

© 2022 The Author(s). Published by the Royal Society of Chemistry

Open Access Article. Published on 11 May 2022. Downloaded on 2/2/2023 7:07:33 AM.
This article is licensed under a Creative Commons Attribution-NonCommercial 3.0 Unported Licence.

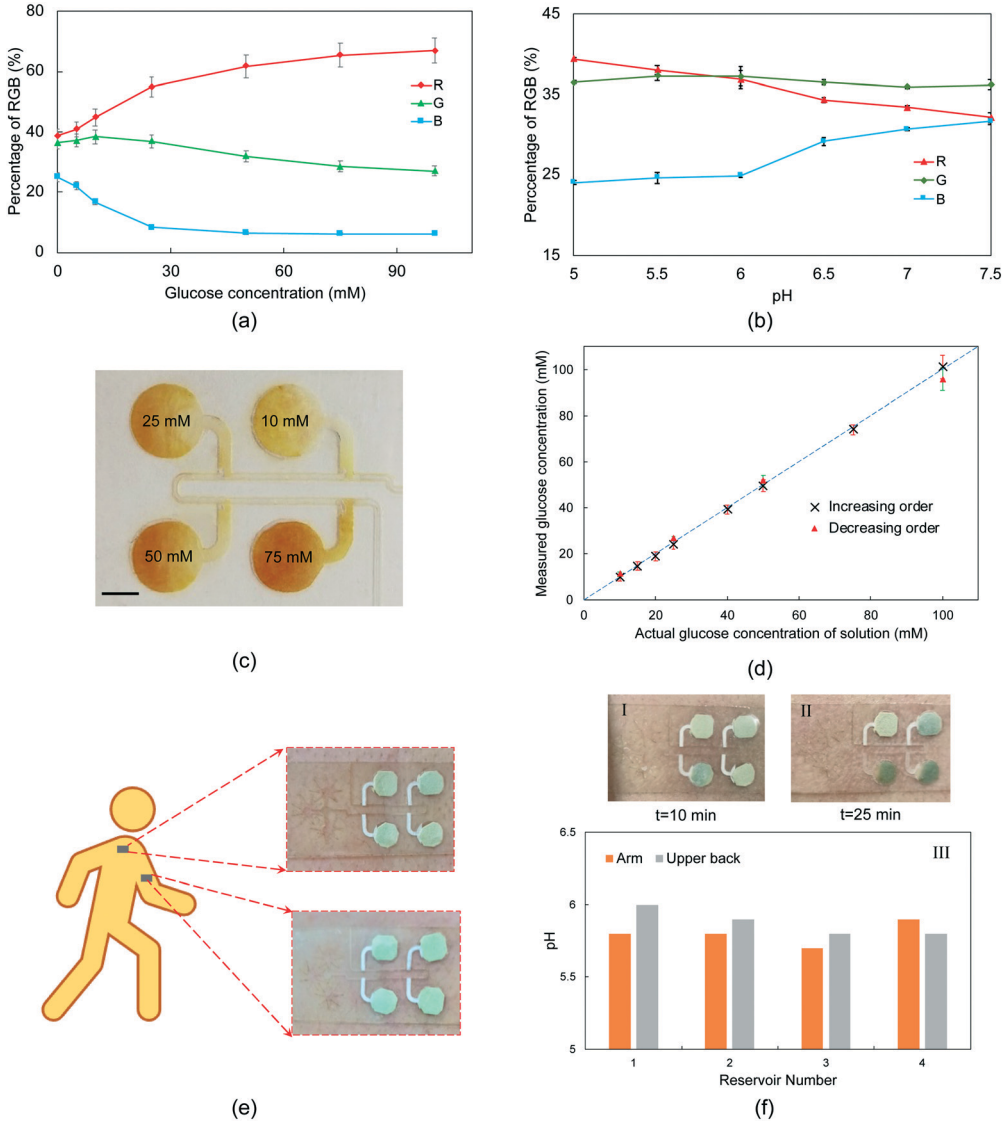


Fig. 6 Quantitative colorimetric analysis of glucose concentration at different standard solutions and determining pH levels under exercise conditions. Calibration plot of normalized R, G, and B values *versus* (a) glucose concentration and (b) pH level. (c) Photograph of the colorimetric analysis of glucose solutions from the chrono-sampling device at a liquid flow rate of 0.5 μL min^{-1} (scale bar is 3 mm). (d) Measured glucose concentrations by chemical analysis *versus* actual solution concentrations. (e) Images of the microfluidic device with inserted pH indicators applied to the arm and upper back of the volunteer. (f) Optical images of the collected sweat from the upper back after (I) 10 min and (II) 25 min, (III) chrono-analysis of the sweat pH.

B channels, corresponding to different glucose solution concentrations. A calibration plot of digital color data (in % RGB format) *versus* glucose concentrations is shown in Fig. 6(a). For glucose assay, the enzymatic reaction of iodide to iodine in the presence of glucose oxidase leads to a change in the color of the substrate from yellow to brown, whose intensity is defined by the concentration of glucose.[46]

To demonstrate the applicability of the proposed microfluidic device under *in vivo* conditions, the developed patch was attached to the arm and upper back of a volunteer under exercise conditions. After sweat collections, the color of the inserted indicator paper in the reservoir changed. A similar approach to glucose experiments was adopted to obtain the calibration plot (Fig. 6(b)).

First, the glucose solutions with concentrations of 10–100 mM were pumped (flow rate of 0.5 μL min^{-1}) into the microfluidic device in a way that the chambers were filled with increasing concentrations of solutions. Although these concentrations are above the physiological levels of glucose in sweat and interstitial fluid, here the goal is to show the functionality of the device in sequential sampling of different glucose concentrations using capillary action. In our future studies, electrochemical sensing will be integrated into the developed microfluidic device in order to analyze lower concentrations of glucose. Additionally, this microfluidic device can be integrated with a microneedle patch to measure the glucose levels in the extracted ISF that has higher concentrations of glucose compared to sweat.[56] Fig.

Open Access Article. Published on 11 May 2022. Downloaded on 2/2/2023 7:07:33 AM.
This article is licensed under a Creative Commons Attribution-NonCommercial 3.0 Unported Licence.

S6† shows the required time for each reservoir to be filled. 23.9 min was needed for all the reservoirs to be filled at a liquid flow rate of 0.5 μL min^{-1}. Although this flow rate is low compared to perspiration rate under exercise conditions or in a sauna, it is considerably higher than sweat rates when the body is at rest. The required times in Fig. S6† suggest that it could take about a day for the reservoirs of 6 mm to be filled during rest. This time would be even longer if the evaporation rate is considered. To address this issue, the diameter of the reservoirs could be decreased. Fig. 6(c) illustrates that the device could successfully guide the solutions of different concentrations into separate reservoirs. In another experiment, the glucose solutions were pumped into the device in a decreasing order to show the functionality of the device under various time-dependent conditions. In Fig. 6(d), the digital images' measured glucose concentrations by the colorimetric analysis were compared with the standard concentrations. As can be seen, there is a good agreement between actual and predicted glucose concentrations. Also, the device showed good reproducibility over a wide range of liquid flow rates (0.1 to 10 μL min^{-1}) with a relative standard deviation of up to 3.5% (Fig. S7,† n = 3), which highlights the effectiveness of the developed approach in wearable applications. The underestimation or overestimation of the glucose content could be because of the lower accuracy of calorimetric analysis compared to other methods such as electrochemical sensing.[6,18] Additionally, a slight intermixing of solutions with different concentrations could be the reason for the inaccurate predictions in the 2nd, 3rd, and 4th reservoirs.

Fig. 6(e) shows optical images of the microfluidic device attached to the arm and upper back of the subject. It is evident from the images that the device bound tightly to the skin, facilitating a conformal, water-tight seal to the skin. The deployed device did not cause any irritation or discomfort during exercise for the subject. The microfluidic patch successfully collected sweat without showing any leakage or detachment. As can be seen in Fig. 6(f), it took 10 and 25 min for the sweat to arrive in the first and third reservoirs, respectively. According to Fig. 6(f)-III, there was no substantial variation in the pH levels during exercise from both arm and upper back, showing a low sweat rate of the subject.[46]

Although the results show negligible leaching during sequential sampling of the glucose solutions, this could be a problematic issue during colorimetric analysis by lowering the homogeneity of the color.[32,57] Since the presented device is designed in a way that each reservoir becomes saturated before the liquid advances, this effect is minimized. The color gradient is lower compared to that of previous studies.[44,45] To further decrease the color gradient, smaller reservoirs could be designed so that the filter papers become saturated quicker. Blocking any further liquid introduction into the chamber will prevent the reagents from being carried along with the glucose solution, which is the main cause of the color gradient. According to previous studies, selecting the proper paper type or using chitosan or silica nanoparticles to cover the paper could reduce the color gradient during glucose detection.[44,58,59] This issue could be decreased more by integrating electrochemical sensing into the microfluidic device. Since each reservoir is completely filled before the liquid starts flowing towards the next reservoir, the sample in each reservoir cannot be refreshed and as a result each reservoir could be used once for biomarker analysis. This potential drawback could be partially addressed by increasing the size of the device, lowering the diameter of the reservoirs, and design optimization, resulting in an increased number of reservoirs. The proposed device is fabricated using low-cost materials (double-sided tape, PET, and filter paper). When all the reservoirs of a device are filled for biomarker analysis, the used device could be replaced easily with a new one.

Conclusions

This study introduces a flexible paper-integrated microfluidic device for sequential capture and analysis of biomarkers in biofluids. The device leverages the high capillary force of filter papers to route the liquid into microreservoirs. The proposed approach does not need an air outlet for each reservoir, leading to more accurate measurements of biomarker concentrations, which are susceptible to evaporation. The results reveal the capability of the designed device in chrono-sampling of liquid at flow rates of up to 5 μL min^{-1}, which could be even higher by changing the design of the microchannels and the dimensions of embedded filter papers. Colorimetric analysis of the sequentially pumped glucose solutions at different concentrations and *in vivo* experiments of pH levels demonstrated that the presented approach could serve as a simple method to monitor temporal variations of physiological state throughout a period of interest.

Experimental

Materials and methods

The wearable device for chrono-analysis of sweat is composed of several layers, which can be listed as (from bottom to top): skin adhesive (60 μm thick; 1524; 3M, MN, USA), transparent polyethylene terephthalate (PET) layer (40 μm thick, MG Chemicals, Canada), microfluidic layer for embedding filter papers (170 μm thick double-sided tape, 9495LE 300LSE, 3M, MN, USA), filter papers (MN 619; Macherey-Nagel, Düren, Germany), and another 40 μm thick PET layer for encapsulation. A laser-cutting machine (Protolaser U4; LPKF, Germany) was used to create the microchannels and reservoirs on the double-sided tape and create the inlet regions on the PET and skin adhesive layers. The design layouts for laser cutting of double-sided tapes and PET layers were prepared using AutoCAD. These layers were vertically assembled to fabricate the microfluidic module. The microfluidic layer contains collection chambers with a

© 2022 The Author(s). Published by the Royal Society of Chemistry

Open Access Article. Published on 11 May 2022. Downloaded on 2/2/2023 7:07:33 AM.
This article is licensed under a Creative Commons Attribution-NonCommercial 3.0 Unported Licence.

diameter and height of 6 mm and 170 μm, respectively (Fig. S1†), resulting in about 5 μL liquid capacity. The chemical assays for colorimetric analysis of glucose concentration were spotted on the reservoir part of the filter papers, followed by inserting the papers in the microfluidic layer. Then, the top and bottom of the microfluidic layer were enclosed by adhering PET layers to the double-sided tape, rendering a 3D microfluidic structure. The medical grade acrylate adhesive is bonded to the bottom microfluidic device, serving as a water-tight interface to the skin.

Forming the colorimetric assay and calibration

Glucose detection involves a chemical reaction of glucose oxidase (Gox; G2133-10KU; Sigma Aldrich, MO, USA) and potassium iodide (KI, Sigma Aldrich, MO, USA). GOx solution was prepared by dissolving 1 mg of glucose oxidase in a 1 mL phosphate buffer solution (PBS). The glucose assay was established by dispensing 5 μL of KI solution (0.6 M) and introducing 5 μL of GOx solution on the filter papers.[55] Then, the filter papers were completely dried, and 5 μL of standard glucose solutions, which were prepared by dissolving glucose powder (D(+)-glucose; 1191GR500; neoFroxx, Germany) at different concentrations, were added to the analytical zone. For pH measurements, commercial indicator paper (REF 92120; Macherey-Nagel, Düren, Germany) served as the assay. A razor blade was used to cut the paper into the desirable shape to facilitate insertion of paper into the reservoirs. After chemical reaction and change of color, the RGB composition of each assay was recorded to be used for the calibration process. Three replicates per measurement were assessed.

Image analysis

The images of the device were captured *via* a smartphone under white light conditions and processed using ImageJ software. After transferring the JPEG images to a computer, R, G, and B channels were extracted and the intensity values of the entire filter paper in each reservoir were measured. The R channel of the images was used to correlate the intensity to the glucose concentration and pH in each reservoir.

Contact angle measurement

5 μL droplets of deionized water were placed on different locations of the surface to measure the contact angle using an Attension® Theta Lite optical tensiometer. The final contact angle of the surface was obtained by measuring and averaging five sessile contact angles.

Author contributions

TA developed the microfluidic device, designed and performed the experiments, acquired and analysed the data, and wrote the manuscript. FM and EI assisted in the device fabrication and data characterization, respectively. HCK reviewed the manuscript and provided comments. LB supervised the project and reviewed the manuscript. All authors approved the final manuscript.

Conflicts of interest

There are no conflicts to declare.

Acknowledgements

T. A., F. M., and L. B. are supported by The Scientific and Technological Research Council of Turkey (TÜBITAK) through 2232 (#118C295) and 2244 (#118C155) programs. L. B. acknowledges the support through a Marie Skłodowska-Curie Individual Fellowship (H2020-MSCA-IF-2018-840786).

References

1 W. Gao, S. Emaminejad, H. Y. Y. Nyein, S. Challa, K. Chen, A. Peck, H. M. Fahad, H. Ota, H. Shiraki and D. Kiriya, *Nature*, 2016, **529**, 509–514.
2 J. Heikenfeld, *Electroanalysis*, 2016, **28**, 1242–1249.
3 G. Matzeu, L. Florea and D. Diamond, *Sens. Actuators, B*, 2015, **211**, 403–418.
4 Y. Yang, Y. Song, X. Bo, J. Min, O. S. Park, L. Zhu, M. Wang, J. Tu, A. Kogan, H. Zhang, T. K. Hsiai, Z. Li and W. Gao, *Nat. Biotechnol.*, 2020, 217–224.
5 L. B. Baker, J. B. Model, K. A. Barnes, M. L. Anderson, S. P. Lee, K. A. Lee, S. D. Brown, A. J. Reimel, T. J. Roberts, R. P. Nuccio, J. L. Bonsignore, C. T. Ungaro, J. M. Carter, W. Li, M. S. Seib, J. T. Reeder, A. J. Aranyosi, J. A. Rogers and R. Ghaffari, *Sci. Adv.*, 2020, **6**, 3929–3940.
6 A. J. Bandodkar, W. J. Jeang, R. Ghaffari and J. A. Rogers, *Annu. Rev. Anal. Chem.*, 2019, **12**, 1–22.
7 D. B. Dill and D. L. Costill, *J. Appl. Physiol.*, 1974, **37**, 247–248.
8 L. E. Gibson and R. E. Cooke, *Pediatrics*, 1959, **23**, 545–549.
9 Y. Zhang, H. Guo, S. B. Kim, Y. Wu, D. Ostojich, S. H. Park, X. Wang, Z. Weng, R. Li, A. J. Bandodkar, Y. Sekine, J. Choi, S. Xu, S. Quaggin, R. Ghaffari and J. A. Rogers, *Lab Chip*, 2019, **19**, 1545–1555.
10 V. F. Curto, C. Fay, S. Coyle, R. Byrne, C. O'Toole, C. Barry, S. Hughes, N. Moyna, D. Diamond and F. Benito-Lopez, *Sens. Actuators, B*, 2012, **171**, 1327–1334.
11 M. J. Patterson, S. D. R. Galloway and M. A. Nimmo, *Acta Physiol. Scand.*, 2002, **174**, 41–46.
12 J. Moyer, D. Wilson, I. Finkelshtein, B. Wong and R. Potts, *Diabetes Technol. Ther.*, 2012, **14**, 398–402.
13 D. A. Kidwell and F. P. Smith, *Forensic Sci. Int.*, 2001, **116**, 89–106.
14 K. B. Hammond, N. L. Turcios and L. E. Gibson, *J. Pediatr.*, 1994, **124**, 255–260.
15 S. B. Kim, Y. Zhang, S. M. Won, A. J. Bandodkar, Y. Sekine, Y. Xue, J. Koo, S. W. Harshman, J. A. Martin, J. M. Park, T. R. Ray, K. E. Crawford, K. T. Lee, J. Choi, R. L. Pitsch, C. C. Grigsby, A. J. Strang, Y. Y. Chen, S. Xu, J. Kim, A. Koh, J. S. Ha, Y. Huang, S. W. Kim and J. A. Rogers, *Small*, 2018, **14**, 1–11.

Open Access Article. Published on 11 May 2022. Downloaded on 2/2/2023 7:07:33 AM.
This article is licensed under a Creative Commons Attribution-NonCommercial 3.0 Unported Licence.

16 M. Chung, G. Fortunato and N. Radacsi, *J. R. Soc., Interface*, 2019, **16**, 20190217.
17 X. Huang, Y. Liu, K. Chen, W. Shin, C. Lu, G. Kong, D. Patnaik, S. Lee, J. F. Cortes and J. A. Rogers, *Small*, 2014, **10**, 3083–3090.
18 Y. Liu, M. Pharr and G. A. Salvatore, *ACS Nano*, 2017, **11**, 9614–9635.
19 J. Choi, D. Kang, S. Han, S. B. Kim and J. A. Rogers, *Adv. Healthcare Mater.*, 2017, **6**, 1–10.
20 Q. Cao, B. Liang, T. Tu, J. Wei, L. Fang and X. Ye, *RSC Adv.*, 2019, **9**, 5674–5681.
21 Z. Zhang, M. Azizi, M. Lee, P. Davidowsky, P. Lawrence and A. Abbaspourrad, *A versatile, cost-effective, and flexible wearable biosensor for in situ and ex situ sweat analysis, and personalized nutrition assessment*, 2019, vol. 19, p. 3448.
22 F. J. Zhao, M. Bonmarin, Z. C. Chen, M. Larson, D. Fay, D. Runnoe and J. Heikenfeld, *Lab Chip*, 2020, **20**, 168–174.
23 Y.-C. Chen, S.-S. Shan, Y.-T. Liao and Y.-C. Liao, *Lab Chip*, 2021, 2524–2533.
24 G. Xiao, J. He, X. Chen, Y. Qiao, F. Wang, Q. Xia, L. Yu and Z. Lu, *Cellulose*, 2019, 4553–4562.
25 U. Mogera, H. Guo, M. Namkoong, M. S. Rahman, T. Nguyen and L. Tian, *Sci. Adv.*, 2022, **8**, 1736.
26 X. Weng, Z. Fu, C. Zhang, W. Jiang and H. Jiang, *Anal. Chem.*, 2022, **94**, 3526–3534.
27 H. Lin, J. Tan, J. Zhu, S. Lin, Y. Zhao, W. Yu, H. Hojaiji, B. Wang, S. Yang and X. Cheng, *Nat. Commun.*, 2020, **11**, 1–12.
28 S. Anastasova, B. Crewther, P. Bembnowicz, V. Curto, H. M. Ip, B. Rosa and G. Z. Yang, *Biosens. Bioelectron.*, 2017, **93**, 139–145.
29 Z. Yao, P. Coatsworth, X. Shi, J. Zhi, L. Hu, R. Yan, F. Gueder and H.-D. Yu, *Sensors & Diagnostics*, 2022, 312–342.
30 A. Vaquer, E. Barón and R. de la Rica, *ACS Sens.*, 2022, **7**, 488–494.
31 Y. Zhang, Y. Chen, J. Huang, Y. Liu, J. Peng, S. Chen, K. Song, X. Ouyang, H. Cheng and X. Wang, *Lab Chip*, 2020, **20**, 2635–2645.
32 J. Choi, A. J. Bandodkar, J. T. Reeder, T. R. Ray, A. Turnquist, S. B. Kim, N. Nyberg, A. Hourlier-Fargette, J. B. Model and A. J. Aranyosi, *ACS Sens.*, 2019, **4**, 379–388.
33 H. Y. Y. Nyein, M. Bariya, B. Tran, C. H. Ahn, B. J. Brown, W. Ji, N. Davis and A. Javey, *Nat. Commun.*, 2021, **12**, 1–13.
34 J. T. Reeder, J. Choi, Y. Xue, P. Gutruf, J. Hanson, M. Liu, T. Ray, A. J. Bandodkar, R. Avila and W. Xia, *Sci. Adv.*, 2019, **5**, eaau6356.
35 T. R. Ray, M. Ivanovic, P. M. Curtis, D. Franklin, K. Guventurk, W. J. Jeang, J. Chafetz, H. Gaertner, G. Young, S. Rebollo, J. B. Model, S. P. Lee, J. Ciraldo, J. T. Reeder, A. Hourlier-Fargette, A. J. Bandodkar, J. Choi, A. J. Aranyosi, R. Ghaffari, S. A. McColley, S. Haymond and J. A. Rogers, *Sci. Transl. Med.*, 2021, **13**(587), eabd8109.
36 N. A. S. Taylor and C. A. Machado-Moreira, *Extrem. Physiol. Med.*, 2013, **2**, 1–30.
37 J. Choi, Y. Xue, W. Xia, T. R. Ray, J. T. Reeder, A. J. Bandodkar, D. Kang, S. Xu, Y. Huang and J. A. Rogers, *Lab Chip*, 2017, **17**, 2572–2580.
38 H. Lim, A. T. Jafry and J. Lee, *Molecules*, 2019, **24**, 2869.
39 E. W. Washburn, *Phys. Rev.*, 1921, **17**, 273.
40 S. Whitaker, *Transp. Porous Media*, 1986, **1**, 3–25.
41 S. M. Hassanizadeh and W. G. Gray, *Water Resour. Res.*, 1993, **29**, 3389–3405.
42 B. J. Toley, B. McKenzie, T. Liang, J. R. Buser, P. Yager and E. Fu, *Anal. Chem.*, 2013, **85**, 11545–11552.
43 E. Fu, S. A. Ramsey, P. Kauffman, B. Lutz and P. Yager, *Microfluid. Nanofluid.*, 2011, **10**, 29–35.
44 E. Evans, E. F. M. Gabriel, W. K. T. Coltro and C. D. Garcia, *Analyst*, 2014, **139**, 2127–2132.
45 S. V. de Freitas, F. R. de Souza, J. C. Rodrigues Neto, G. A. Vasconcelos, P. V. Abdelnur, B. G. Vaz, C. S. Henry and W. K. T. Coltro, *Anal. Chem.*, 2018, **90**, 11949–11954.
46 A. Koh, D. Kang, Y. Xue, S. Lee, R. M. Pielak, J. Kim, T. Hwang, S. Min, A. Banks, P. Bastien, M. C. Manco, L. Wang, K. R. Ammann, K. I. Jang, P. Won, S. Han, R. Ghaffari, U. Paik, M. J. Slepian, G. Balooch, Y. Huang and J. A. Rogers, *Sci. Transl. Med.*, 2016, **8**(366), 366ra165.
47 A. A. S. Bhagat, E. T. K. Peterson and I. Papautsky, *J. Micromech. Microeng.*, 2007, **17**, 1017.
48 H. M. Xia, S. Y. M. Wan, C. Shu and Y. T. Chew, *Lab Chip*, 2005, **5**, 748–755.
49 Z. Sonner, E. Wilder, J. Heikenfeld, G. Kasting, F. Beyette, D. Swaile, F. Sherman, J. Joyce, J. Hagen, N. Kelley-Loughnane and R. Naik, *Biomicrofluidics*, 2015, **9**, 31301.
50 X. Fu, B. Xia, B. Ji, S. Lei and Y. Zhou, *Anal. Chim. Acta*, 2019, **1065**, 64–70.
51 J. H. Shin, J. Park, S. H. Kim and J.-K. Park, *Biomicrofluidics*, 2014, **8**, 54121.
52 S. B. Kim, K. Lee, M. S. Raj, B. Lee, J. T. Reeder, J. Koo, A. Hourlier-Fargette, A. J. Bandodkar, S. M. Won and Y. Sekine, *Small*, 2018, **14**, 1802876.
53 H. Yin Yin Nyein, L.-C. Tai, Q. P. Ngo, M. Chao, G. B. Zhang, W. Gao, M. Bariya, J. Bullock, H. Kim, H. M. Fahad and A. Javey, *ACS Sens.*, 2018, **3**, 944–952.
54 P. Salvo, F. Di Francesco, D. Costanzo, C. Ferrari, M. G. Trivella and D. De Rossi, *IEEE Sens. J.*, 2010, **10**, 1557–1558.
55 X. He, T. Xu, Z. Gu, W. Gao, L.-P. Xu, T. Pan and X. Zhang, *Anal. Chem.*, 2019, **91**, 4296–4300.
56 P. P. Samant and M. R. Prausnitz, *Proc. Natl. Acad. Sci. U. S. A.*, 2018, **115**, 4583–4588.
57 G. G. Morbioli, T. Mazzu-Nascimento, A. M. Stockton and E. Carrilho, *Anal. Chim. Acta*, 2017, **970**, 1–22.
58 E. F. M. Gabriel, P. T. Garcia, T. M. G. Cardoso, F. M. Lopes, F. T. Martins and W. K. T. Coltro, *Analyst*, 2016, **141**, 4749–4756.
59 E. Evans, E. F. M. Gabriel, T. E. Benavidez, W. K. T. Coltro and C. D. Garcia, *Analyst*, 2014, **139**, 5560–5567.

© 2022 The Author(s). Published by the Royal Society of Chemistry